cmgh
CELLULAR AND MOLECULAR GASTROENTEROLOGY AND HEPATOLOGY

ORIGINAL RESEARCH

Perivascular Interstitial Cells of Cajal in Human Colon

Yuan-An Liu,[1] Yuan-Chiang Chung,[2] Ming-Yin Shen,[3] Shien-Tung Pan,[4] Chun-Wei Kuo,[5] Shih-Jung Peng,[1,6] Pankaj J. Pasricha,[7,*] and Shiue-Cheng Tang[1,6,*]

[1]Connectomics Research Center, National Tsing Hua University, Hsinchu, Taiwan; [2]Department of Surgery, Cheng Ching General Hospital, Chung Kang Branch, Taichung, Taiwan; [3]Division of Colorectal Surgery, National Taiwan University Hospital, Hsinchu Branch, Hsinchu, Taiwan; [4]Department of Pathology, Miaoli General Hospital, Miaoli, Taiwan; [5]Department of Pathology, National Taiwan University Hospital, Hsinchu Branch, Hsinchu, Taiwan; [6]Department of Medical Science, National Tsing Hua University, Hsinchu, Taiwan; [7]Division of Gastroenterology and Hepatology, Johns Hopkins University School of Medicine, Baltimore, Maryland

SUMMARY

This work explores the association between interstitial cells of Cajal (ICC) and the microvascular network in the human colon wall using a novel high-definition three-dimensional microscopic approach. The authors propose the existence of a new subclass of ICC, the perivascular ICC.

BACKGROUND & AIMS: Interstitial cells of Cajal (ICC) closely associate with nerves and smooth muscles to modulate gut motility. In the ICC microenvironment, although the circulating hormones/factors have been shown to influence ICC activities, the association between ICC and microvessels in the gut wall has not been described. We applied three-dimensional (3D) vascular histology with c-kit staining to identify the perivascular ICC and characterize their morphologic and population features in the human colon wall.

METHODS: Full-thickness colons were obtained from colectomies performed for colorectal cancer. We targeted the colon wall away from the tumor site. Confocal microscopy with optical clearing (use of immersion solution to reduce scattering in optical imaging) was performed to simultaneously reveal the ICC and vascular networks in space. 3D image rendering and projection were digitally conducted to illustrate the ICC–vessel contact patterns.

RESULTS: Perivascular ICC were identified in the submucosal border, myenteric plexus, and circular and longitudinal muscles via high-definition 3D microscopy. Through in-depth image projection, we specified two contact patterns—the intimate cell body-to-vessel contact (type I, 18% of ICC in circular muscle) and the long-distance process-to-vessel contact (type II, 16%)—to classify perivascular ICC. Particularly, type I perivascular ICC were detected with elevated c-kit staining levels and were routinely found in clusters, making them readily distinguishable from other ICC in the network.

CONCLUSIONS: We propose a new subclass of ICC that closely associates with microvessels in the human colon. Our finding suggests a functional relationship between these mural ICC and microvessels based on the morphologic proximity. *(Cell Mol Gastroenterol Hepatol 2015;1:102–119; http://dx.doi.org/10.1016/j.jcmgh.2014.11.003)*

Keywords: 3D Histology; c-kit; ICC; Mural Cells.

In the colon as well as other parts of the digestive tract, interstitial cells of Cajal (ICC) integrate with nerves and muscles as part of the machinery to regulate motility.[1–3] In the gut wall, ICC form a three-dimensional (3D) network to associate with circular and longitudinal muscles and generate/propagate slow waves to maintain spontaneous peristaltic movements.[4] Although the slow-wave activity has been shown to be influenced by both the neuronal inputs[5,6] and circulating hormones,[7,8] the signal transduction pathway of the latter—that is, from the hormones to ICC—is poorly understood. In an attempt to establish the connection, lines of evidence have emerged to indicate that ICC may be directly influenced by the intestinal hormones: (1) the expression of the gut hormone cholecystokinin receptors on ICC[9] and (2) the discovery of serotonin receptors 5-HT_3 and 5-HT_4 on ICC by immunohistochemistry.[10,11] Particularly, regarding the serotonin pathway, although the source of serotonin and the function(s) of the 5-HT receptors on ICC are unclear, the receptors are hypothesized to participate in the slow wave initiation and/or alteration based on their known functions.[12]

In addition to modulating the slow-wave activity, circulating hormones and factors have also been shown to maintain the population of ICC in the gut wall. For example, the signaling pathway initiated by the binding of the stem cell factor (SCF) to its receptor tyrosine kinase c-kit is essential for the ICC development and survival.[13] Mice with SCF deficiency, loss-of-function mutation of c-kit, or administration of the anti-c-kit antibody suffered from the loss of ICC network and/or function.[14–16] On the other hand, activation of the 5-HT_{2B} receptor on ICC by serotonin has been shown to increase the ICC proliferation in vitro, while

*Authors contributed equally.

Abbreviations used in this paper: 3D, three-dimensional; 5-HT, serotonin; ICC, interstitial cells of Cajal; ICC-SM, ICC at the submucosal border; ICC-CM, ICC in the circular muscle; ICC-MY, ICC around the myenteric plexus; ICC-LM, ICC in the longitudinal muscle; NA, numerical aperture; PBS, phosphate-buffered saline; SCF, stem cell factor.

2352-345X
http://dx.doi.org/10.1016/j.jcmgh.2014.11.003

lack of this activation reduced the density of ICC in adult mice.[17,18]

Based on the established and suggested influences of circulating molecules on ICC (including cholecystokinin, serotonin, SCF, insulin, and insulin-like growth factor-1[19]), study of the ICC microenvironment ideally should include the vasculature to integrate the local ICC microenvironment with the circulation. From a therapeutic perspective, examining the vascular network around ICC provides an opportunity to evaluate the efficiency of therapeutic agents to reach ICC through blood vessels in treating motility disorders such as diabetic gastroparesis[20,21] and slow transit constipation[22,23] or stromal tumors with c-kit mutation.[24,25] However, reports concerning the interaction between ICC and blood vessels are lacking. This is largely because of the dispersed nature of the ICC and vascular networks, which cannot be easily portrayed by the standard microtome-based two-dimensional histology to characterize their spatial relationship.

To visualize the intestinal tissue networks, we previously developed a penetrative 3D imaging method based on preparation of transparent tissues with optical clearing[26–28]—a technique of using a solution of high refractive index to improve light transmission in optical microscopy[29,30]—to characterize the enteric nervous system and ICC with high definition.[31–34] Using the same approach, we also examined the microvessels in the human colorectal carcinoma to characterize their morphologic and density changes from those in the normal tissues.[35] In this research, we simultaneously targeted the ICC and vascular networks using paired c-kit and CD31 immunostaining to reveal their association in the human colon wall. Importantly, a new subclass of ICC, the perivascular ICC, is presented in this report with qualitative and quantitative analyses to identify their unique features and population density. The physiologic implications of the mural ICC are discussed.

Materials and Methods

Human Specimens

Collection and use of human tissues were approved by the institutional review board of National Taiwan University Hospital, Hsinchu Branch, with written consent from the patients to use the obtained tissues. Colonic tissues were obtained from colectomies performed for nonobstructive carcinoma. Samples of normal muscularis were obtained at least 5 cm apart from the carcinoma. The removed tissues were first perfused with phosphate-buffered saline (PBS) through the mesenteric artery to flush the residual blood and then with ice-cold 4% paraformaldehyde for 30 minutes for fixation. Afterward, the tissues were postfixed in 4% paraformaldehyde solution overnight at 4°C before being transferred to 0.1% paraformaldehyde for preservation. Specimens were later sectioned to 300 μm in thickness by vibratome before being applied for tissue labeling.

Tissue Labeling

The fixed specimens were immersed in 2% Triton X-100 solution for 2 hours at 15°C for permeabilization. The primary antibodies used to reveal ICC were a monoclonal rabbit anti-c-kit antibody (cat. no. 1522–1; Epitomics, Burlingame, CA) and a polyclonal rabbit anti-Ano1 antibody (also known as anti-TMEM16A, cat. no. ab53212; Abcam, Cambridge, MA). A monoclonal mouse anti-CD31 antibody (cat. no. MS-353-S1; Thermo Scientific, Fremont, CA) was used to reveal the vasculature.

Before we applied the antibodies, the tissue was rinsed in PBS. This was followed by a blocking step, incubating the tissue with the blocking buffer (2% Triton X-100, 10% normal goat serum, and 0.02% sodium azide in PBS). The primary antibodies were then diluted in the dilution buffer (1:100, 0.25% Triton X-100, 1% normal goat serum, and 0.02% sodium azide in PBS) to replace the blocking buffer and incubated overnight at 15°C. Alexa-Fluor

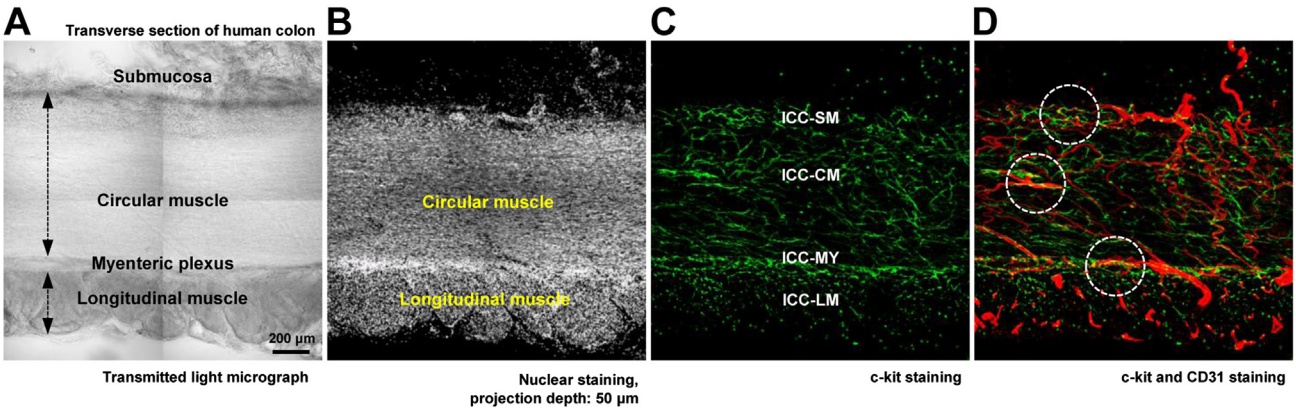

Figure 1. Deep-tissue microscopy of colonic muscularis reveals ICC-vasculature association. (*A* and *B*) Layers of human colonic wall in transverse section. Specimens were optically cleared to improve light transmission. The transmitted light and nuclear signals derived from in-depth microscopy outline the tissue microstructure. (*C* and *D*) ICC subgroups and their association with vasculature. Merged projection of ICC (c-kit$^+$) and vasculature (CD31$^+$) reveals the locations with apparent overlap of the two network systems (*circles*). ICC-CM, ICC in the circular muscle; ICC-MY, ICC around the myenteric plexus; ICC-LM, ICC in the longitudinal muscle; ICC-SM, ICC at the submucosal border. *A–D* were derived from the same image stack.

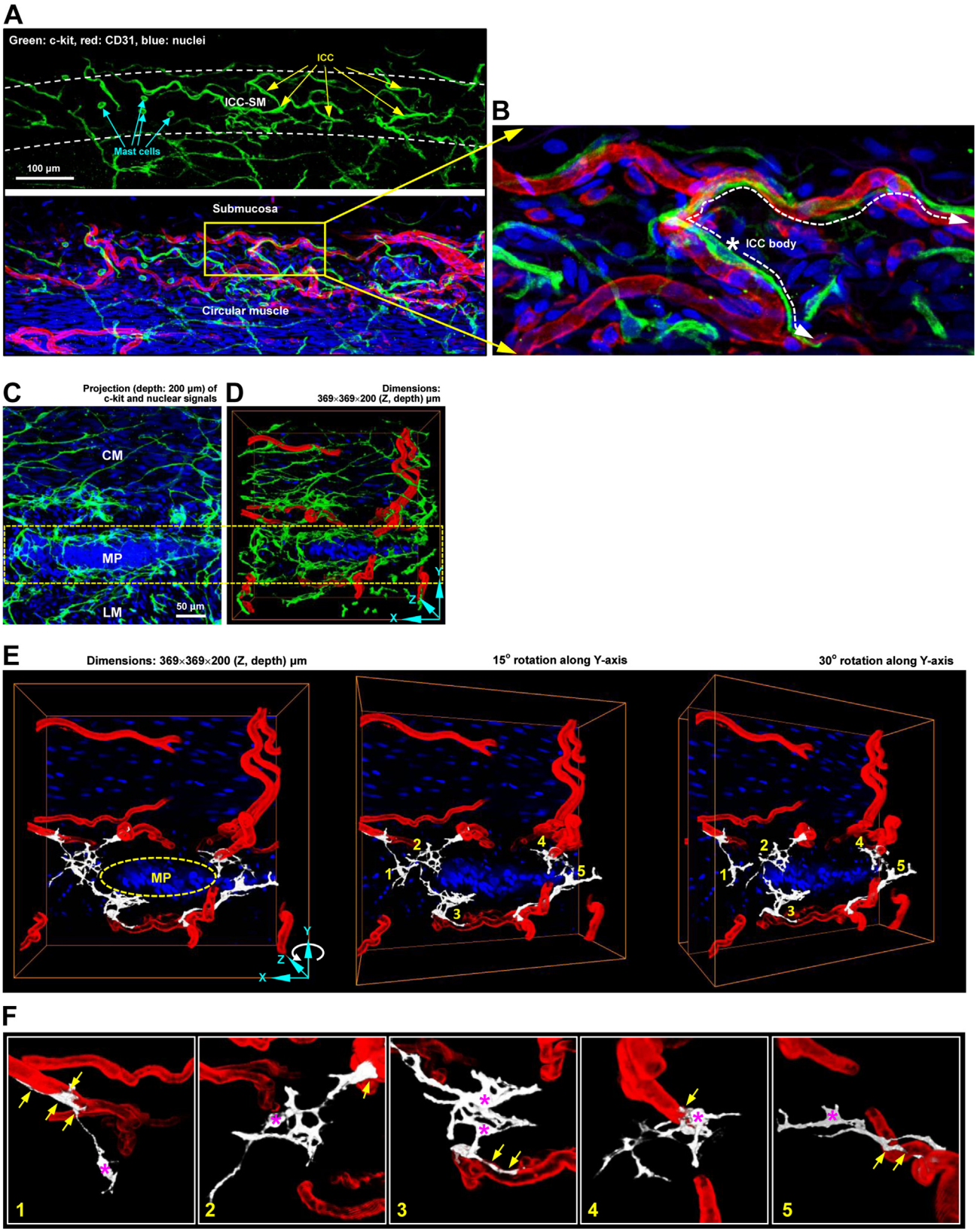
A
Green: c-kit, red: CD31, blue: nuclei
ICC
ICC-SM
Mast cells
100 μm
Submucosa
Circular muscle
B
ICC body
C
Projection (depth: 200 μm) of c-kit and nuclear signals
CM
MP
LM
50 μm
D
Dimensions: 369×369×200 (Z, depth) μm
E
Dimensions: 369×369×200 (Z, depth) μm
15° rotation along Y-axis
30° rotation along Y-axis
MP
F
1
2
3
4
5

647-conjugated goat anti-rabbit secondary antibody and Alexa-Fluor 546-conjugated goat anti-mouse secondary antibody (1:200; Invitrogen, Carlsbad, CA) were used to reveal the immunostained structures. Afterward, nuclear staining by SYTO16 (4 μmol/L; Invitrogen) was performed at 15°C for 1 hour. The labeled specimens were then immersed in the optical clearing solution FocusClear (CelExplorer, Hsinchu, Taiwan) before being imaged via confocal microscopy.

Confocal Microscopy

A Zeiss LSM510 Meta confocal microscope (Carl Zeiss, Jena, Germany) equipped with 10× Fluar objective lenses (numerical aperture [NA]: 0.5) was used to acquire the gross view of the ICC network (Figure 1, tile-scanning mode: 2 × 2 image stacks; optical section: 10 μm; *z*-axis increment: 5 μm). The 40× LD C-Apochromat water immersion lenses (NA: 1.1; working distance: 620 μm; optical section: 2 or 3 μm; *z*-axis increment: 1 or 1.5 μm) were used to acquire the detailed ICC and vascular features. The 25× LD Plan-Apochromat glycerin immersion lenses (NA: 0.8; working distance: 570 μm; optical section: 5 μm; *z*-axis increment: 2.5 μm) were used to acquire the image stacks for ICC quantitation. The laser-scanning process was operated under the multitrack scanning mode to sequentially acquire signals in multiple channels, including the transmitted light channel. The Alexa Fluor 647-labeled tissue structures were excited at 633 nm, and the fluorescence was collected by the 650- to 710-nm band-pass filter. The Alexa Fluor 546-labeled tissue structures were excited at 543 nm, and the signals were collected by the 560- to 615-nm band-pass filter. The SYTO16 signals were excited at 488 nm, and the fluorescence was collected by the 500- to 550-nm band-pass filter.

Image Processing and Projection

The Avizo 6.2 image reconstruction software (VSG, Burlington, MA; operated under a Dell T7500 workstation), the Zen software (Carl Zeiss), and the LSM510 software (Carl Zeiss) were used for processing, projection, and analysis of the confocal image stacks. Avizo's noise-filtering algorithms were applied for background noise reduction. Signal tracing, image segmentation, and feature extraction were performed by the Label Field function of Avizo.[34] The Voltex module and the Camera Rotate function of Avizo were applied for the panoramic display of ICC and vascular networks in Figures 2*D–F*, 3*C–F*, 4*D–F*, and 5, and Supplementary Videos 1–3, 5, and 6. Supplementary Video 4 was recorded via the Orthoslice and Animation functions of Avizo. Figures 1*B–D*, 2*A–C*, 4*A–C*, 6*A–D*, 10*C–E*, and 11*B* and *C* were derived from the 3D projection module of the LSM510 software.

Image Analysis

Quantitation of ICC was performed using the image stacks derived from the transverse sections of circular muscle. The Landmark function of the Avizo software was applied to digitally mark and count the ICC in the image stack. ICC were defined as the c-kit-positive cells with at least two processes extending from the cell body, which was specified by the c-kit enclosed nuclear signal. Supplementary Video 4 gives an example of identifying the type I and type II perivascular ICC based on the contact patterns between c-kit and CD31 signals. Overall, 59 image stacks were used in quantitation (Table 1). The c-kit staining levels of different ICC subclasses were assessed by the Histogram module of the Zen software with a 50-μm projection depth to estimate the fluorescence signal intensities.

Statistical Analysis

The results are expressed as mean ± standard deviation. The data of the intrasubject ICC subgroups were evaluated by unpaired Student *t* test (Figure 6*E*). Data of intersubject ICC subgroups were evaluated by regression analysis. $P < .05$ was considered statistically significant.

Regression Analysis

Description. We conducted a regression analysis on the ICC of the six subjects to assess whether type I perivascular ICC are indeed brighter than the other two ICC subgroups. In the analysis, we regress the c-kit staining levels on dummy variables for type I, type II, and the six subjects using the ICC not associated with blood vessels in Subject A as the benchmark group (ie, the mean c-kit staining level for this benchmark group is a0).

Regression Equation. c-kit staining level = a0 + a1 * TypeI + a2 * TypeII + b1 * SubjectB + b2 * SubjectC + b3 * SubjectD + b4 * SubjectE + b5 * SubjectF + error

Coefficients.

a0: Intercept term of the regression

a1: Regression coefficient for the variable "Type I perivascular ICC"

a2: Regression coefficient for the variable "Type II perivascular ICC"

b1: Regression coefficient for the variable "Subject B"

…

b5: Regression coefficient for the variable "Subject F"

Figure 2. (***See previous page***). **Perivascular ICC in colonic submucosal boundary and myenteric plexus.** (*A* and *B*) Perivascular ICC at the submucosal border. The (*A*) tissue map and (*B*) zoom-in examination of ICC at the submucosal border identify the perivascular ICC with its cell body and processes following the microvessels in space. Projection depth: 60 μm. (*C* and *D*) Perivascular ICC around the myenteric ganglion. An in-depth projection of ICC, vasculature, and nuclear signals identifies the myenteric ganglion (*yellow box*) and its surrounding ICC and microvessels. (*D*) The nuclear signals were placed at the background to help locate the myenteric ganglion. (*E* and *F*) Zoom-in examination of ICC-vessel contacts around myenteric ganglion. Signals of five ICC-MY (numbers 1–5; enlarged in *F*) were extracted from *D* to highlight the periganglionic ICC-vessel contacts. The five ICC-MY were also recorded and projected from different angles in Supplementary Video 1 to illustrate their spatial association with microvessels. *Yellow arrows* in *F* are the ICC-vessel contacts. *Asterisks* denote ICC cell bodies. CM, circular muscle; LM, longitudinal muscle; MP, myenteric plexus; MY, myenteric plexus.

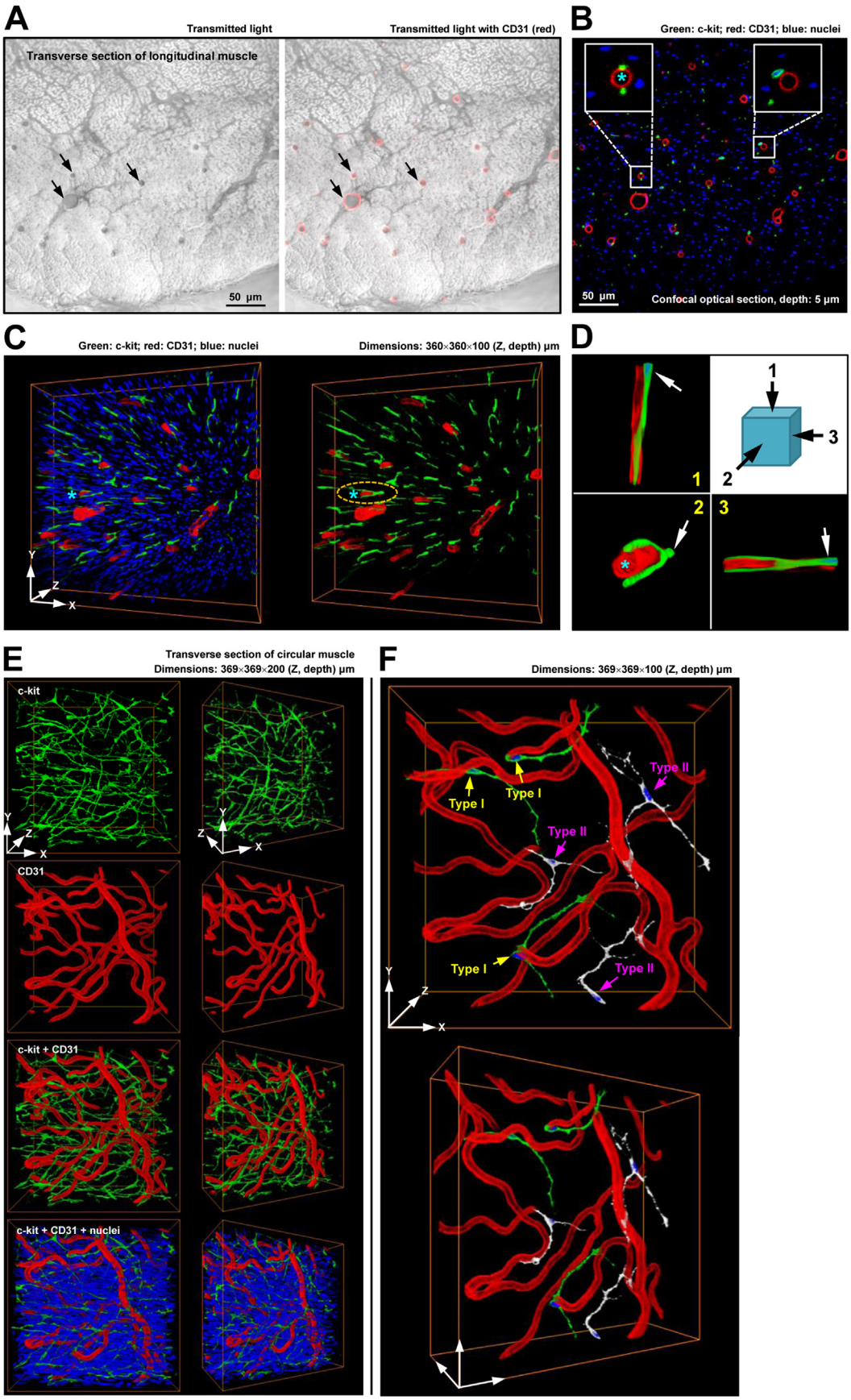
A
Transmitted light
Transmitted light with CD31 (red)
Transverse section of longitudinal muscle
50 μm
B
Green: c-kit; red: CD31; blue: nuclei
50 μm
Confocal optical section, depth: 5 μm
C
Green: c-kit; red: CD31; blue: nuclei
Dimensions: 360×360×100 (Z, depth) μm
D
E
Transverse section of circular muscle
Dimensions: 369×369×200 (Z, depth) μm
c-kit
CD31
c-kit + CD31
c-kit + CD31 + nuclei
F
Dimensions: 369×369×100 (Z, depth) μm
Type I
Type II

error: The error term of the regression, with mean 0

Variables.

c-kit staining level: Expressed as percentage of signal saturation (as shown in Figure 6*E*)

TypeI: A dummy variable of 1 if the ICC is Type I, and 0 otherwise

TypeII: A dummy variable of 1 if the ICC is Type II, and 0 otherwise

SubjectB: A dummy variable of 1 if the ICC is from Subject B, and 0 otherwise

…

SubjectF: A dummy variable of 1 if the ICC is from Subject F, and 0 otherwise

Estimation Results.

Cell type adjustment

a0 = 41.32% (t-stat = 32.90)

a1 = 9.81% (t-stat = 7.30)

a2 = 2.80% (t-stat = 1.98)

Individual adjustment

b1 = 8.88% (t-stat = 5.71)

b2 = 8.99% (t-stat = 4.93)

b3 = 7.25% (t-stat = 4.13)

b4 = 8.40% (t-stat = 4.62)

b5 = −1.44% (t-stat = −0.80)

Tests of Hypotheses. *Hypothesis 1:* a1 = 0 (Type I perivascular ICC and ICC not associated with blood vessels have the same c-kit staining level.)

Result: t-stat = 7.30 → Reject Hypothesis 1 at the 1% level.

Hypothesis 2: a2 = 0 (Type II perivascular ICC and ICC not associated with blood vessels have the same c-kit staining level.)

Result: t-stat = 1.98 → Reject Hypothesis 2 at the 5% level.

Hypothesis 3: a1 − a2 = 0 (Type I and type II have the same c-kit staining level.)

Result: F-stat = 16.06 → Reject Hypothesis 3 at the 1% level.

Conclusions of Regression Analysis. The estimate of a1 is 9.8% (t-stat = 7.30), indicating that the type I perivascular ICC are on average 9.8% brighter than the ICC not associated with blood vessels, after accounting for differences across subjects. The difference is statistically significant at the 1% level.

The estimate of a2 is 2.8% (t-stat = 1.98), indicating that the type II perivascular ICC are on average 2.8% brighter than the ICC not associated with blood vessel. The difference is statistically significant at the 5% level.

The result also indicates that the type I perivascular ICC are on average 7.0% brighter than the type II perivascular ICC. The difference (9.8%–2.8%) is statistically significant at the 1% level (result of *F* test), with a F-stat of 16.06.

The three ICC subgroups (type I perivascular ICC, type II perivascular ICC, and ICC not associated with blood vessels) are significantly different in the c-kit staining levels.

Results

Deep-Tissue Microscopy of Interstitial Cells of Cajal and Vascular Networks

To visualize the ICC and vascular networks in space, we prepared transparent human colon specimens by optical clearing to reveal the c-kit and CD31-labeled structures via deep-tissue microscopy. Figure 1 shows the submucosa, circular muscle, myenteric plexus, and longitudinal muscle and their associated ICC populations—the ICC at the submucosal border (ICC-SM), ICC in the circular muscle (ICC-CM), ICC around the myenteric plexus (ICC-MY), and ICC in the longitudinal muscle (ICC-LM)—in these domains. Importantly, through merged projection of c-kit and CD31 signals (Figure 1*D*), locations with the apparent overlap of the ICC and vascular networks were revealed in the tissue map.

Perivascular Interstitial Cells of Cajal in the Submucosal Border and Myenteric Plexus Populations

Zooming into the submucosal boundary, Figure 2*A* and *B* shows a subgroup of ICC-SM closely following the microvessel in space. The cell body and processes of the perivascular ICC contact the vascular walls, showing their intimacy. The perivascular ICC can be distinguished from the c-kit$^+$ mast cells (Figure 2*A*) because the latter lack the prolonged processes to connect other ICC in the plexus.

An association between ICC and microvessels was also observed in the myenteric plexus (Figure 2*C* and *D*). A zoom-in examination of the myenteric ganglion revealed that a subclass of ICC-MY positioned their cell bodies around the ganglion with the processes extending to and docking on the walls of the periganglionic microvessels (Figure 2*E* and *F*, and Supplementary Video 1).

Perivascular Interstitial Cells of Cajal in Longitudinal Muscle

In addition to the ICC-SM and ICC-MY, the perivascular ICC can also be found in the ICC populations in the longitudinal

Figure 3. (***See previous page***). **Perivascular ICC in colonic smooth muscles.** (*A*–*D*) Perivascular ICC in the longitudinal muscle. Transmitted light and fluorescence images (*A* and *B*) show the tissue map of the longitudinal muscle. Locations of the CD31$^+$ microvessels were confirmed in *A* (*arrows*). The perivascular c-kit signals were presented in *B* (*boxes*). *Asterisk* indicates the lumen of vessel. The gross view (*C*) and zoom-in projections (*D*, three projection angles, illustrated at the upper-right corner) of the image stack identify the contact of ICC with the microvessel and their extended association in space. The *asterisks* in *C* and *D* indicate the same ICC (*oval*). The *white arrows* in *D* specify the ICC cell body. (*E* and *F*) Perivascular ICC in the circular muscle. Merged (*E*) and segmented (*F*) signal projections of ICC and microvessels identify two types of perivascular ICC: (1) the type I perivascular ICC with cell body-to-vessel contact and (2) the type II perivascular ICC with process-to-vessel contact only. *E* and *F* were derived from the same image stack with panel *F* presenting the perivascular ICC from different angles. The *arrows* indicate the ICC cell bodies (identified by the enclosed nuclear signals, *blue*).

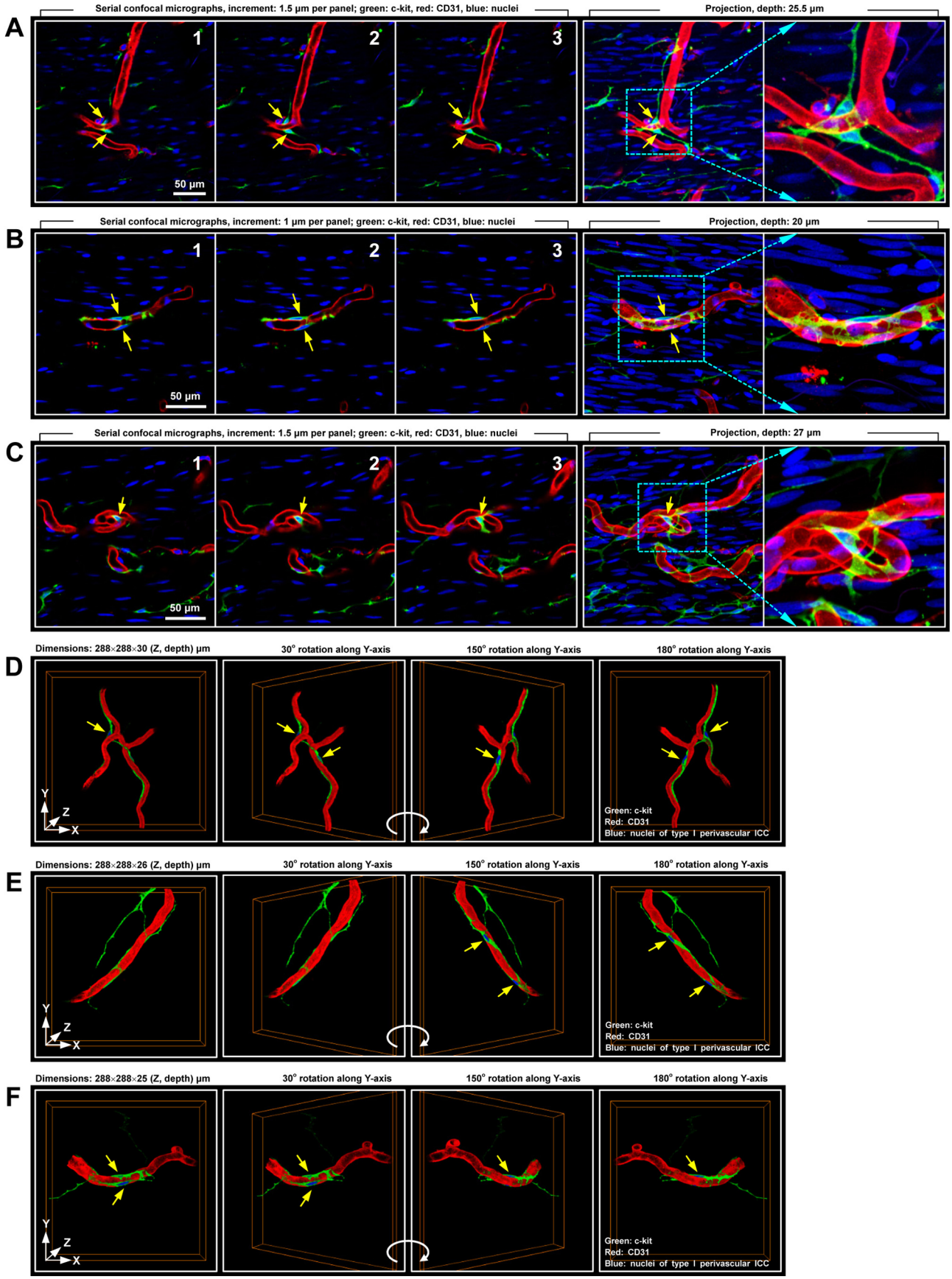
A
Serial confocal micrographs, increment: 1.5 μm per panel; green: c-kit, red: CD31, blue: nuclei
Projection, depth: 25.5 μm
1
2
3
50 μm
B
Serial confocal micrographs, increment: 1 μm per panel; green: c-kit, red: CD31, blue: nuclei
Projection, depth: 20 μm
1
2
3
50 μm
C
Serial confocal micrographs, increment: 1.5 μm per panel; green: c-kit, red: CD31, blue: nuclei
Projection, depth: 27 μm
1
2
3
50 μm
D
Dimensions: 288×288×30 (Z, depth) μm
30° rotation along Y-axis
150° rotation along Y-axis
180° rotation along Y-axis
Y
Z
X
Green: c-kit
Red: CD31
Blue: nuclei of type I perivascular ICC
E
Dimensions: 288×288×26 (Z, depth) μm
30° rotation along Y-axis
150° rotation along Y-axis
180° rotation along Y-axis
Y
Z
X
Green: c-kit
Red: CD31
Blue: nuclei of type I perivascular ICC
F
Dimensions: 288×288×25 (Z, depth) μm
30° rotation along Y-axis
150° rotation along Y-axis
180° rotation along Y-axis
Y
Z
X
Green: c-kit
Red: CD31
Blue: nuclei of type I perivascular ICC

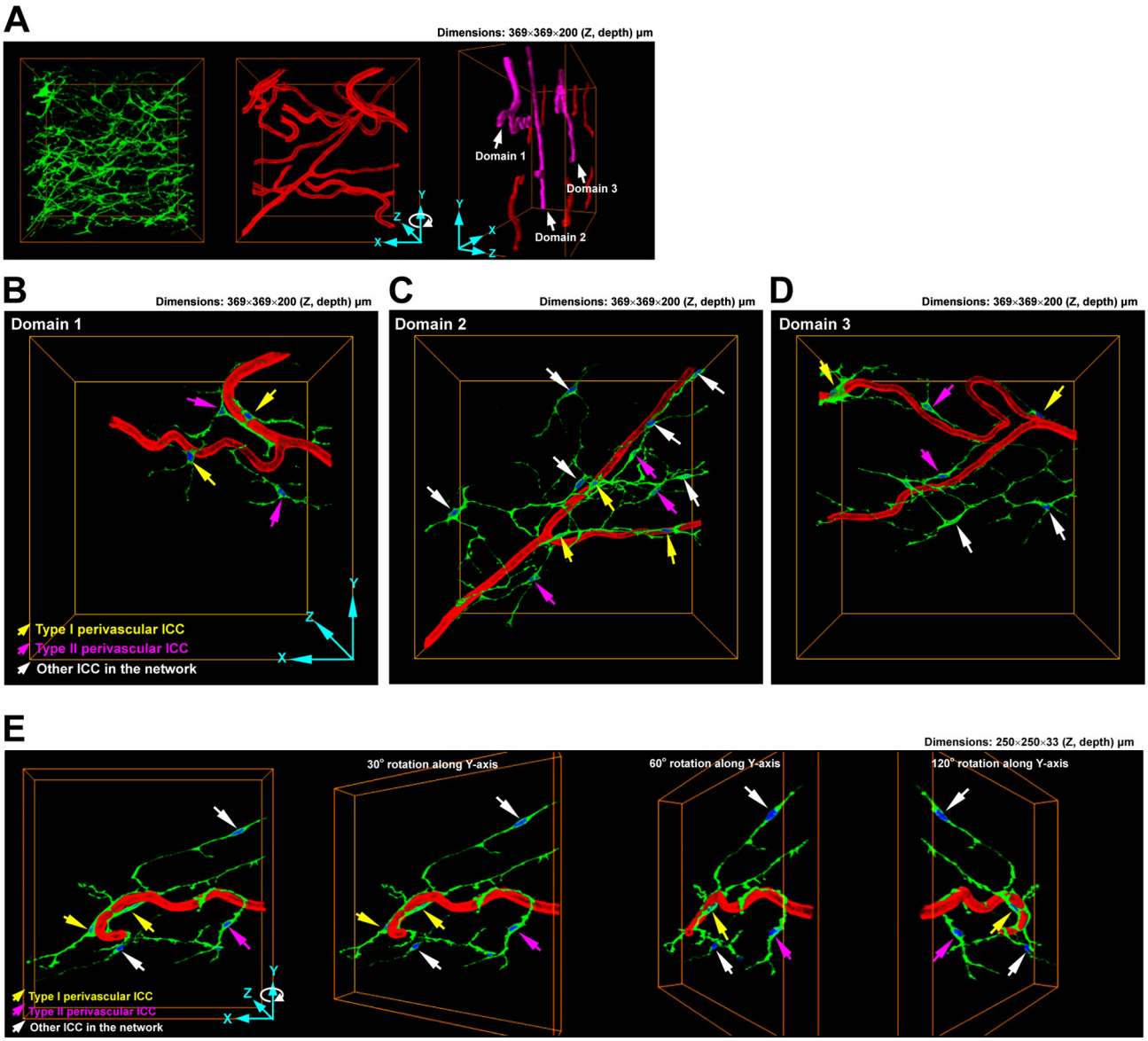

Figure 5. Perivascular ICC in the ICC-CM network. (*A–D*) Gross view and zoom-in examination of ICC and vasculature in circular muscle. Domains 1–3 (*arrows*) were enlarged in *B–D* for detailed examination. Type I and type II perivascular ICC and other ICC in the network were projected in space and specified by *colored arrows*. Panoramic presentation of the image stack was recorded in Supplementary Video 6. (*E*) A second example of the ICC-CM and microvessel integration. The components of the network were labeled by *colored arrows* and visualized from different projection angles.

and circular muscles (Figure 3). Using the transparent longitudinal muscle, we identified the embedded microvessels and the perivascular ICC by overlaying and pairing the transmitted light and fluorescence signals (Figure 3*A* and *B*). Following the focal depth, we specified a subset of the ICC-LM residing on the microvessel wall (Figure 3*C*). Zoom-in examination of the mural ICC confirmed the aligned feature of ICC with microvessels and their extended contacts along the vessel wall (Figure 3*D* and Supplementary Video 2).

Perivascular Interstitial Cells of Cajal in Circular Muscle

Among the different layers/domains of the colon wall, the circular muscle provides the best environment to

Figure 4. (***See previous page***). **Morphologic characterization of type I perivascular ICC.** (*A–C*) Visualization of type I perivascular ICC with high definition. Three examples are presented here. (*A*) Two ICC clamping the microvessel. (*B*) One ICC with the processes embracing the vessel wall. (*C*) One ICC residing at the vessel loop. Sixteen additional examples are presented in Figure 9. (*D–F*) 3D projection and panoramic visualization of type I perivascular ICC. CD31, c-kit, and nuclear signals of type I perivascular ICC were segmented and panoramically projected to highlight the contacts of ICC with microvessels. *Arrows* indicate the ICC cell bodies.

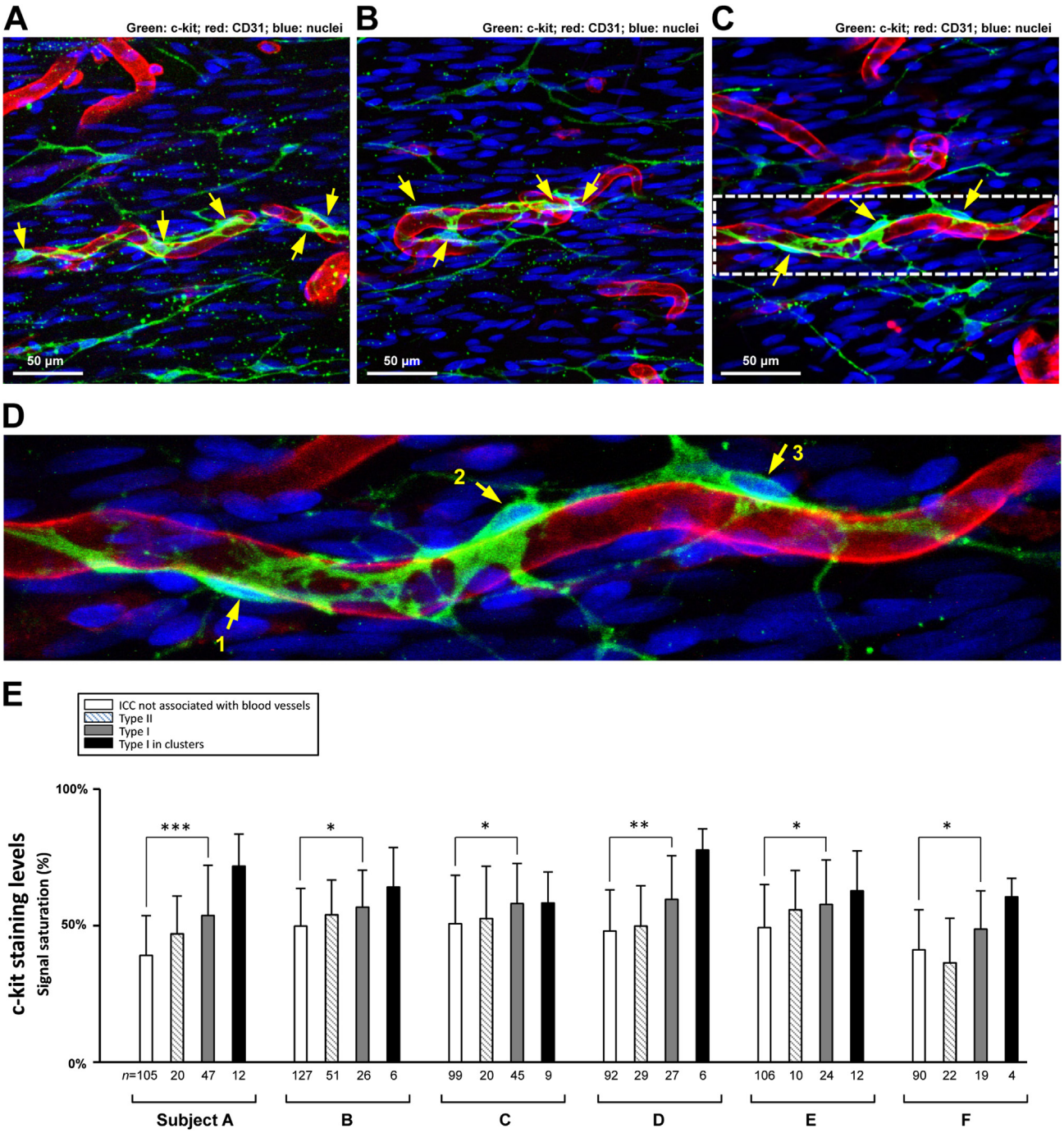

Figure 6. Type I perivascular ICC in clusters and with elevated c-kit staining levels. (*A–D*) Aggregation of type I perivascular ICC. Three examples are presented here. In *C,* the *box* was enlarged in *D* to present the clustered ICC (numbers 1–3) with high definition. *Arrows* indicate the ICC cell bodies on the vessel wall. (*E*) c-kit staining levels in ICC-CM. Quantification (specimens derived from six human subjects) shows that the c-kit staining levels were higher in type I perivascular ICC than in those of the type II and ICC not associated with blood vessels; the difference was statistically significant against the latter. The c-kit levels further increased in the type I perivascular ICC in clusters. Here, n indicates the number of cells analyzed in each subject. $^{*}P < .05$; $^{**}P < .01$; $^{***}P < .001$.

characterize the perivascular ICC because of the defined domain boundary, homogeneity, and large area for examination (Figures 1*A* and *B* and 3*E*). We therefore zoomed into this region and performed qualitative and quantitative analyses of the perivascular ICC to characterize their detailed morphologic and population features.

Before entering the detailed ICC presentation, we would like to stress two aspects of the CD31 immunostaining to specify the revealed vascular structure. First, the CD31 immunohistochemistry identifies the platelet endothelial cell adhesion molecules (or PECAM-1) and thus reveals the endothelial cells of all microvessels, including the capillary,

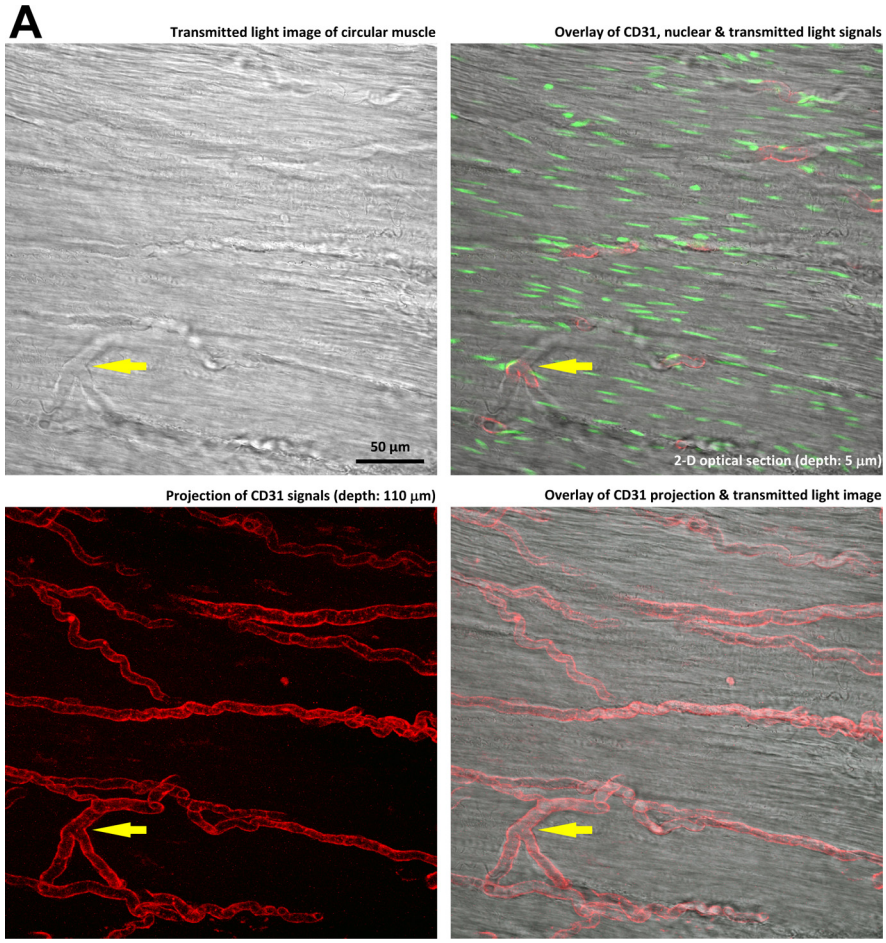

Figure 7. (See Figure 3*F* and Table 1.) Verification of the CD31-labeled microvessels. (*A*) Overlay of transmitted light and confocal micrographs to confirm the CD31-labeled microvessels in circular muscle. Transmitted light image provides the objective information to identify the size and locations of the microvessels. Matched vascular features were seen in both the transmitted light and fluorescence images (such as the bifurcation indicated by the *arrow*). The same approach was used in Figure 3*A* and *B* to identify the $CD31^+$ microvessels in the longitudinal muscle. (*B* and *C*) Comparison of CD31 (also known as platelet endothelial cell adhesion molecule, or PECAM-1) and lymphatic endothelial marker D2-40 labeled vascular structures. (*B*) Shows the tubelike blood vessels in the myenteric plexus and circular and longitudinal muscles. (*C*) Shows the saclike lymphatic vessel (*arrow*) at the periganglionic region in the myenteric plexus. In general, the $D2\text{-}40^+$ lymphatic vessels can be found at the interfaces between the different layers of the colon wall. In comparison, the $CD31^+$ microvessels perfuse the tissue and densely reside at all areas of the colon wall. NOTE. In the circular muscle, we avoided the boundary and focused on the tubelike $CD31^+$ microvessels in the intramuscle region to characterize the detailed features of the perivascular ICC.

arteriole, and venule. Second, similar to the transparent longitudinal muscle (Figure 3*A*), in the transparent circular muscle we used both the transmitted light and CD31 signals to identify the blood vessels (Figure 7*A*) and to distinguish them from the lymphatic vessels (Figure 7*B* and *C*; the latter lack rigid vessel walls and primarily reside around the myenteric plexus against the muscle layers).

In qualitative analysis, Figure 3*F* shows two contact patterns between the ICC and microvessels: (1) the intimate cell body-to-vessel contact and (2) the long-distance process-to-vessel contact. We classify the ICC with the first feature as the type I perivascular ICC (with or without the second feature) and those with the second feature and only the second feature as the type II perivascular ICC. Based on the classification, we quantified the ratios of type I (18.4% ± 2.6%) and type II (15.7% ± 3.7%) perivascular ICC in the ICC-CM population in six individuals (Table 1) (note that the average ICC-CM density derived from the six individuals is 2396 cells/mm^3; ICC are defined as the c-kit-positive cells with at least two processes extending from the cell body).[34] Added together, the overall ratio of the perivascular ICC in ICC-CM was as much as 34.1% (ie, one of three ICC-CM contacting the blood vessels), reflecting the importance of this ICC subgroup in the ICC-CM population. Supplementary Videos 3 and 4 present the ICC analysis in a stereo fashion.

To rule out that the association of ICC with microvessels is due to their random contacts in space, Figure 8

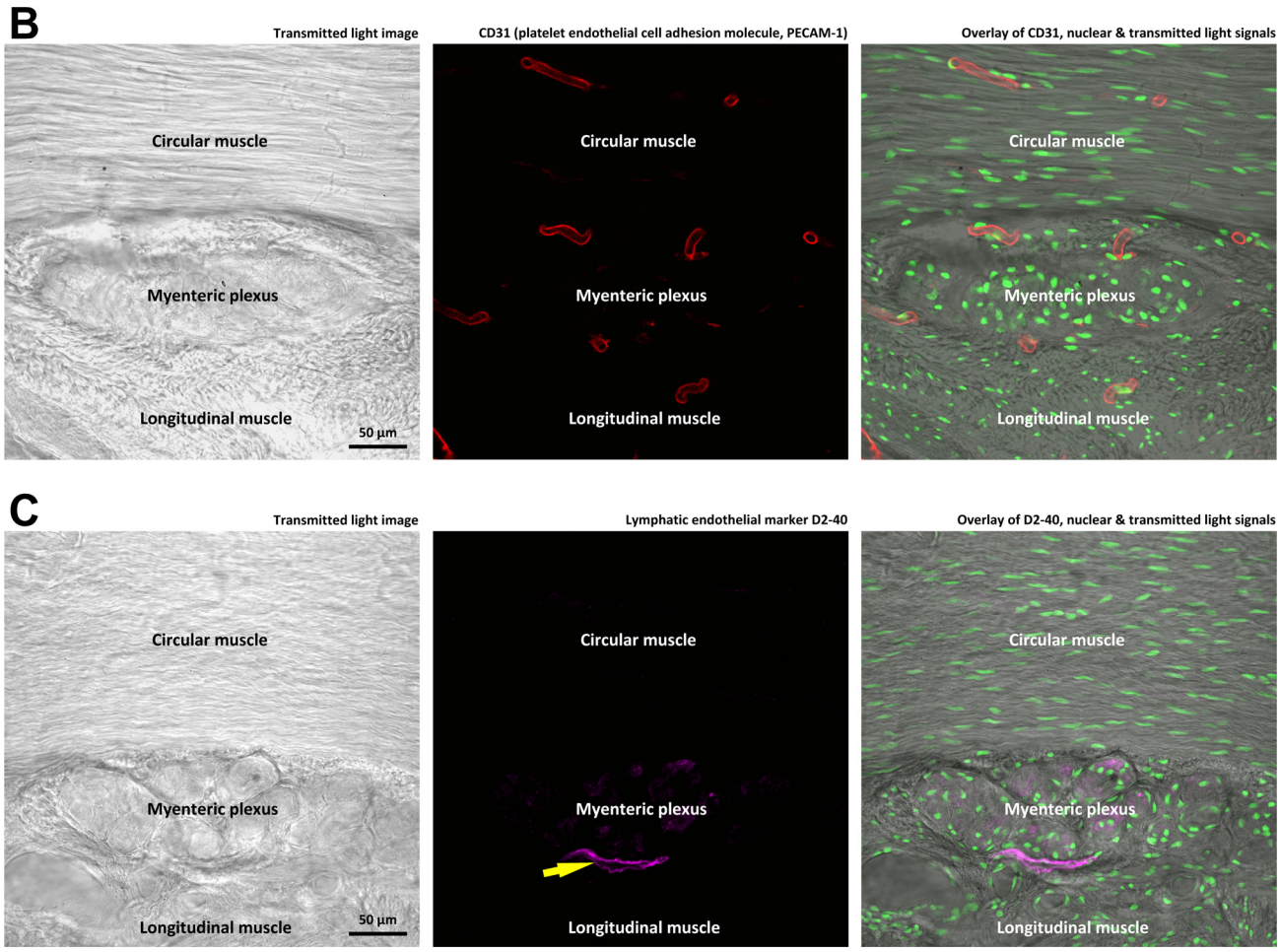

Figure 7. (*continued*).

illustrates our approach to evaluating the potential random contacts of the two tissue networks in space. This test was done by digitally swapping the ICC population (ie, the c-kit signals) between two adjacent image stacks and then examining the ICC-vessel contacts in an arbitrary fashion. In five pairs of these images, only 5.7% of the ICC-CM contacted the microvessels in their arbitrary locations. The ratio was statistically significantly lower than the 34.1% ratio of the perivascular ICC in the ICC-CM ($P < .001$).

Furthermore, Figure 4 zooms into individual type I perivascular ICC to depict the detailed ICC morphologic features around the microvessels. Intimate ICC-vessel associations, such as two ICC clamping the microvessel (Figure 4*A*), processes of ICC embracing the vessel wall (Figure 4*B*), and the ICC residing at the vessel loop (Figure 4*C*), were displayed in projection and from various angles (Figure 4*D–F* and Supplementary Video 5). A gallery of 16 additional projections is presented in Figure 9 to illustrate the ICC-vessel contacts with high definition.

Finally, based on the overlap of the fluorescence signals and the resolving power of confocal microscopy (laser lines at 543 and 633-nm were used in the fluorescence illumination), the span between the perivascular ICC and the vessel wall was estimated to be within 300 nm.

Type I Perivascular Interstitial Cells of Cajal in Clusters and with Elevated c-kit Staining Levels

In addition to the intimate cell body-to-vessel contact, Figure 6 illustrates two additional features of type I perivascular ICC on the microvessels. First, the type I perivascular ICC were routinely found in clusters on the vessel wall (27.0% ± 11.4% of type I perivascular ICC in circular muscle in six subjects). Figure 6*A–D* shows three examples of the ICC cluster on the microvessel with adjacent cell bodies within a span of 50 μm. Second, the type I perivascular ICC were detected with elevated c-kit staining levels in comparison with those of the type II and ICC not associated with blood vessels in the intrasubject ICC analysis (Figure 6*E*; $P < .05$ against the latter, unpaired Student *t* test) and the intersubject regression analysis (see *Regression Analysis*) ($P < .01$ against both groups). Particularly, in five of the six subjects, we observed a further increase in c-kit signals of the clustered type I perivascular ICC, making them readily distinguishable from other ICC in the network.

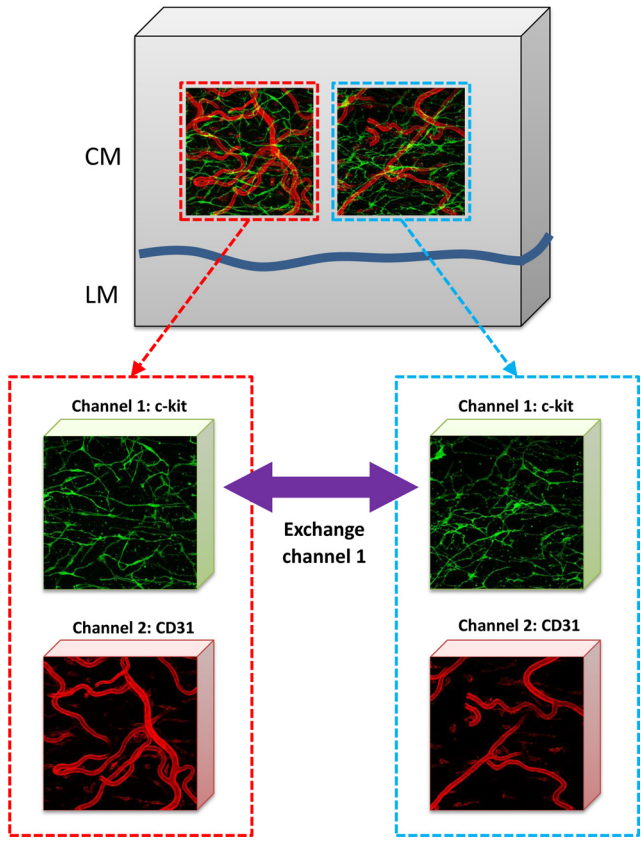

Figure 8. (See Figure 3*E* and *F*.) Schematic illustration of the blind control test of ICC-microvessel random contacts. A pair of image stacks with c-kit-labeled ICC (*green*) and CD31-labeled microvessel (*red*) were first acquired from the adjacent areas in the circular muscle. To create the blind random contacts, the c-kit signals were digitally swapped between the adjacent image stacks using the Avizo software. We then quantified the ICC-vessel contacts at their new arbitrary locations. CM, circular muscle; LM, longitudinal muscle.

Perivascular Interstitial Cells of Cajal in the Circular Muscle Network

Zooming out from the contacts of ICC with blood vessels, Figure 5*A–D* and Supplementary Video 6 show the spatial integration of the perivascular ICC with the entire ICC-CM. Importantly, through in-depth projection, we were able to trace the cell bodies and processes of the perivascular ICC to confirm their coupling with other ICC in space. Figure 5E presents a second example of the cell-cell coupling of ICC from various angles.

In addition to the c-kit-labeled ICC network, Figures 10 and 11 present the Ano1-labeled ICC network to confirm the perivascular ICC. Because the Ano1 expression has been associated with the function of the calcium-dependent chloride channel and the generation of the slow waves,[36–38] the Ano1 immunostaining provides an independent assessment,[39] in addition to the c-kit staining, to specify the perivascular presence of ICC in the circular muscle (Figure 10*E*). Finally, Figure 11 presents the Ano1-labeled ICC imaged with different tissue depths to examine the acquired fluorescence signals. Because the projection depth of the optically cleared tissue (60 μm in Figure 11*C*) is larger than the thickness of a standard tissue section (15 μm in Figure 11*B*), such a difference explains why it appears that more ICC are revealed in our images and videos in comparison with the number of ICC derived from the standard immunohistochemistry.[39]

Overall, the 3D imaging, projection, and quantitation of the perivascular ICC in the human colon identify the integration between the ICC and vascular networks and underline the presence of microvessels in the immediate ICC microenvironment.

Discussion

The classic view of the ICC microenvironment includes the triad of ICC, nerves, and smooth muscles that contribute to the initiation and regulation of the spontaneous peristaltic movements of gut wall.[1–4] In addition to the three

Table 1. Ratio of Perivascular ICC in ICC Population in Circular Muscle

			Perivascular ICC (%)		
Subject	Gender/age (*y*)	Segment	Type I (cell body-to-vessel contact)	Type II (process-to-vessel contact only)	ICC not associated with blood vessels (%)
A	Female/60	Transverse	21.0	12.6	66.4
B	Female/65	Sigmoid	14.7	22.0	63.3
C	Male/43	Sigmoid	19.1	15.0	65.9
D	Male/61	Sigmoid	22.0	18.9	59.1
E	Female/53	Sigmoid	16.0	15.0	69.0
F	Male/63	Ascending	17.9	11.0	71.1

NOTE: Number of ICC counted from each subject: A, n = 438; B, n = 409; C, n = 408; D, n = 428; E, n = 381; and F, n = 391. Density of ICC in circular muscle (ie, sum of the three subclasses of ICC per tissue volume) of each subject: A, 2091 ± 890 cells/mm^3 (n = 14 image stacks); B, 2545 ± 763 cells/mm^3 (n = 8); C, 2063 ± 621 cells/mm^3 (n = 10); D, 2261 ± 416 cells/mm^3 (n = 9); E, 2751 ± 1139 cells/mm^3 (n = 9); and F, 2667 ± 415 cells/mm^3 (n = 8).

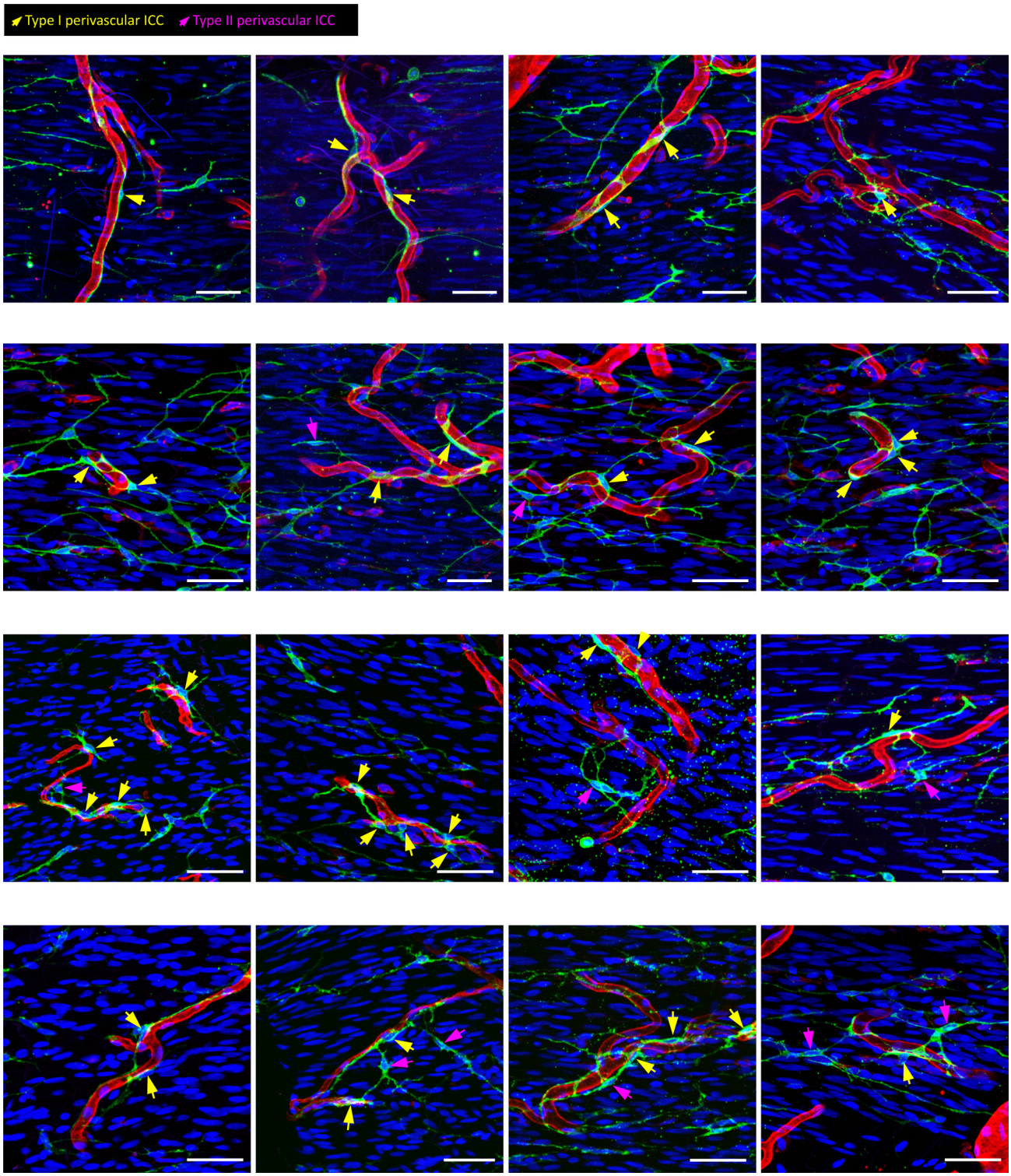

Figure 9. (See Figure 4.) Gallery display of perivascular ICC in circular muscle (16 examples). Cell bodies of the type I and type II perivascular ICC are labeled by *arrows*. *Green*: c-kit. *Red*: CD31. *Blue*: nuclei. *Bar*: 50 μm.

components, in this research we applied high-definition 3D microscopy to identify the vascular network as a fourth component to directly associate with the ICC plexuses in the human colon wall. The association was established by the ICC cell body-to-vessel contact and/or the processes docking on the vessel wall to integrate the two network systems. The intimate ICC-to-vessel association together with their elevated c-kit staining levels and clustering on the vessel wall prompted us to propose a new subclass of ICC, the perivascular ICC, to highlight their unique morphologic features.

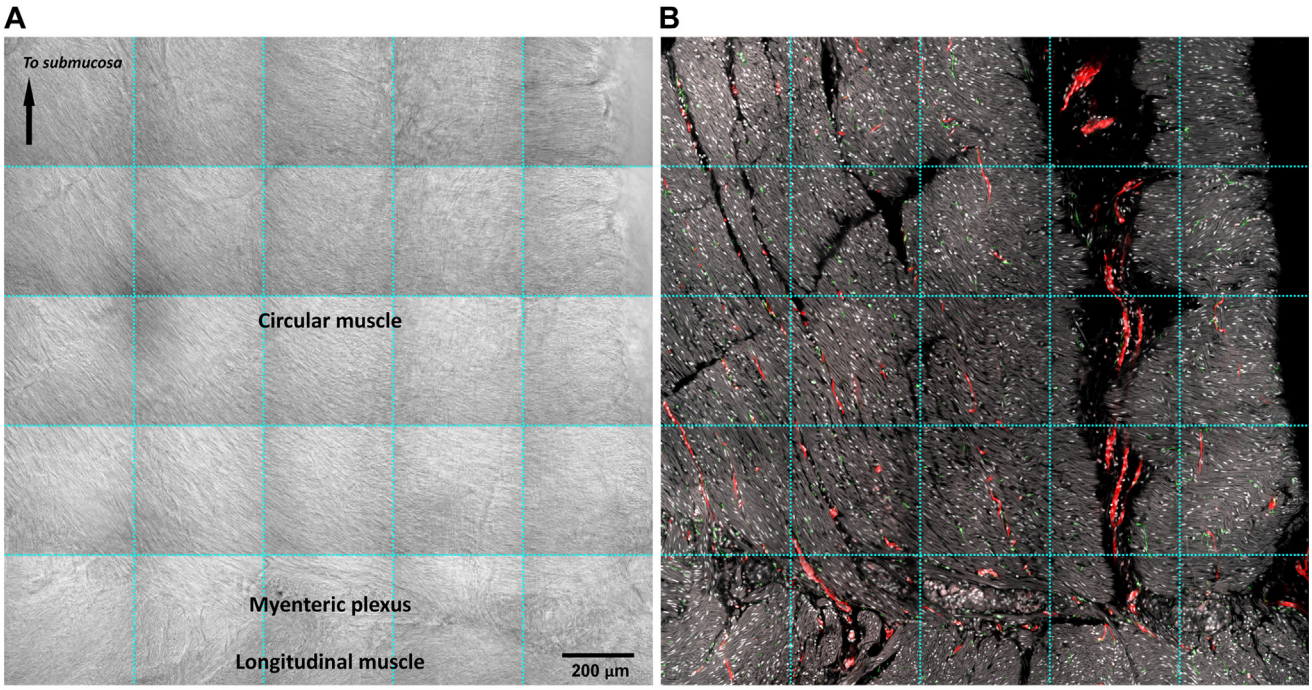

Tile scanning to acquire the tissue map (transmitted light image)

Stitching of 2-D fluorescence micrographs (confocal optical section: 5 μm in thickness)

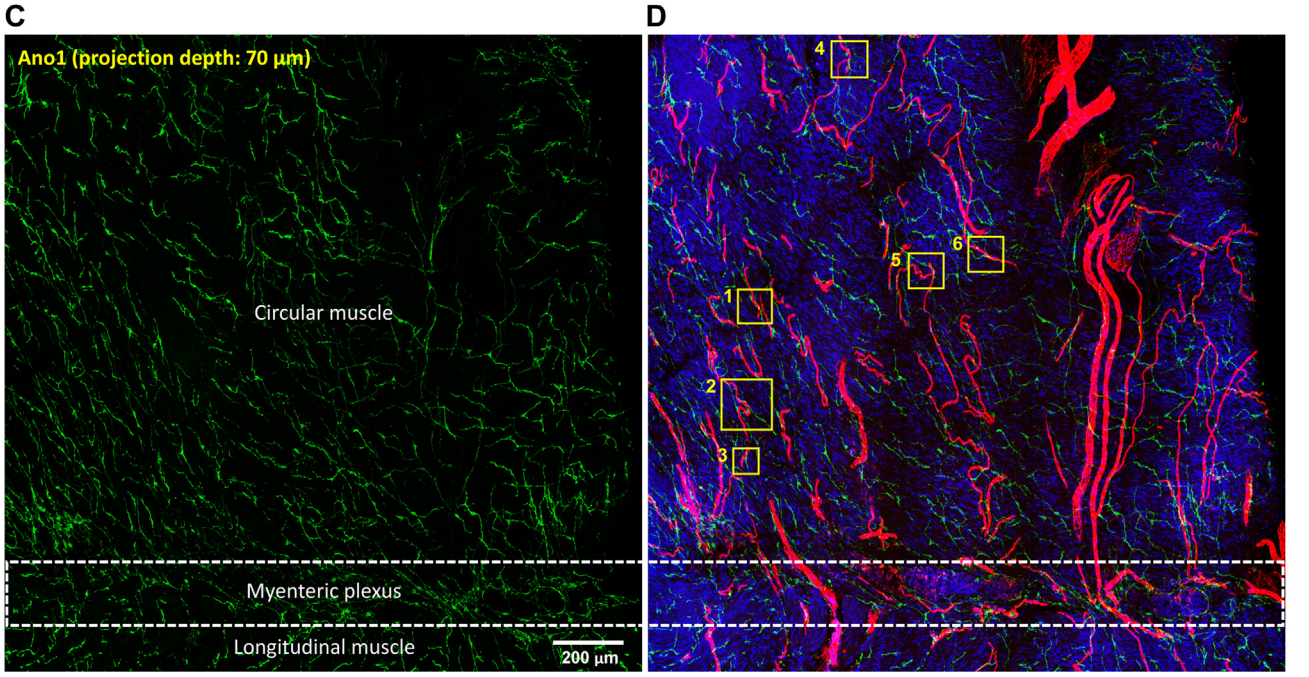

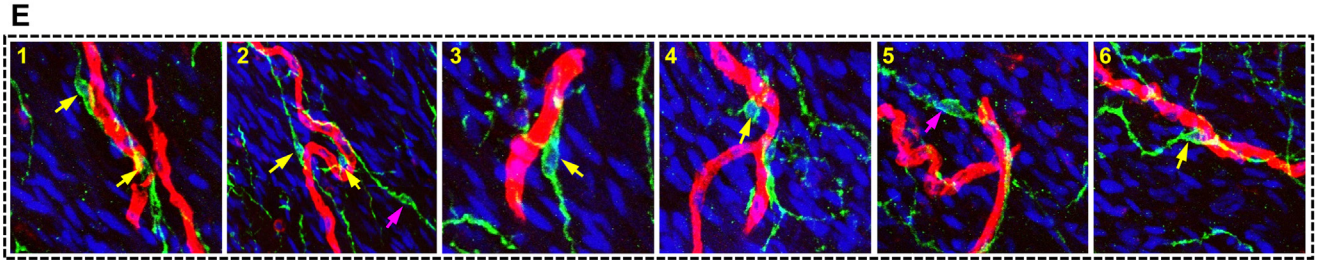

Unlike the conventional ICC classification based on the locations—the ICC-SM, ICC-CM, ICC-MY, and ICC-LM[40–42]—the new ICC-to-vessel classification that we propose emphasizes the contact patterns (Table 1) and the potential vascular influence on the perivascular ICC. The morphologic connection of the ICC plexus to the vascular network supports the concept that ICC rely on both the nervous and circulatory signals to modulate the slow-wave activity in response to physiologic cues. The circulatory pathway thus represents a natural route to target ICC for potential pharmacologic intervention to influence the ICC function.

For the ICC maintenance, however, the situation is complicated by the ICC microenvironment. Our high-definition images reveal that the perivascular ICC are potentially the endothelium-associated anchorage-dependent cells, particularly the type I perivascular ICC, which receive the substratum and likely the c-kit-mediated stimulation from the microvessel (the latter was suggested by the high c-kit staining levels) (Figure 6E). Because chronic diseases such as diabetes and hypertension can cause microvascular injury and/or dysfunction,[43,44] whether the disturbances of microcirculation lead to the remodeling of perivascular ICC and a change of the population density requires further investigation to understand the potential microvascular influence on the ICC function and motility disorders.

The technical advance of preparing the transparent human colon specimens allowed us to use 3D microscopy to simultaneously visualize the ICC and vascular networks in an integrated fashion, which otherwise cannot be easily portrayed by the standard two-dimensional histology. Because of the improved optical condition, we were able to apply transmitted light imaging to identify the domain boundaries and microstructures of the colon wall (Figures 1*A* and 3*A*), which served as the landmarks to confirm the signals derived from fluorescence labeling and confocal microscopy. However, this imaging approach has the following limitations. First, the tissue clearing condition is not compatible with calcium imaging to identify the functional connection between ICC and microvessels. Second, the deep-tissue imaging approach is not compatible with super-resolution microscopy to examine the membrane structures, such as the potential gap junctions between the endothelium and ICC. Use of electron microscopy to characterize the ultrastructure of the perivascular ICC will be needed in the future to further define the cell body (type I) and process (type II) contacts of ICC with the endothelium. Detailed information about the ultrastructure and contact patterns in the context of disease (such as diabetic gastroparesis) will help link the unique anatomy of perivascular ICC with the physiology and pathophysiology of intestine.

Despite the limitations, 3D microscopy with optical clearing has two technical advantages. First, the method is compatible with the standard tissue fixation and labeling procedures, including immunohistochemistry, to identify the tissue structures and networks of interest. Second, the imaging approach is compatible with tile scanning in confocal microscopy for large-area network mapping. These two advantages have made 3D microscopy with optical clearing an important tool in neuroanatomy for the visualization and study of the central and peripheral nervous systems,[45–48] including the enteric nervous system.[31–33]

In characterizing the perivascular ICC, we chose to use the CD31 immunostaining to reveal the microvessels because the marker has been routinely used in the analysis of microvessel density to evaluate the tumor angiogenesis.[49,50] This practice led us to use the same approach to identify the colonic microvessels in this research. In reporting the ratios of the perivascular ICC (Table 1), we assume that the CD31 immunohistochemistry identified most, if not all, of the microvessels in the specimen (Figure 7*A*). However, we do not rule out the possibility that the apparent vessel density would change if a different vascular marker was used, which could in turn influence the estimated ratios of the perivascular ICC.

In quantitation of the c-kit staining levels (Figure 6*E*), it should be noted that the fluorescence signals derived from the c-kit molecules were amplified in the staining and imaging processes. In acquiring the signals, we assumed that the amplification was proportional and minimally influenced by the sensitivity and saturation of the antigen-antibody binding and microscopic detection. In addition, we assumed that the same antibody-to-c-kit binding efficiency was held across the six subjects, although a slightly different ICC population profile appears in subject F in Figure 6*E*.

In summary, we applied 3D microscopy to identify a new subclass of ICC, the perivascular ICC, in the human colon wall. Before this study, the microvascular network had not been demonstrated in the ICC microenvironment. We performed both survey imaging and high-definition microscopy of the colon wall to characterize the morphologic and population features of the perivascular ICC. The discovery of perivascular ICC lays the foundation for future research into the interplay between the ICC and endothelium to increase our understanding of the mechanisms that regulate ICC activity in health and the change of the ICC microenvironment in motility disorders.

Figure 10. (***See previous page***). **Use of paired Ano1 and CD31 immunostaining to verify the presence of perivascular ICC.** (*A–D*) Tissue map of human colonic specimen. *Red*: CD31. *Green*: Ano1. White (*B*)/blue (*D*): nuclear staining and tissue autofluorescence (images acquired at high detector gain). Six regions of the tissue were marked for zoom-in investigation (*boxes* 1–6). (*E*) Ano1-labeled perivascular ICC in projection. *Panels* 1–6 are the zoom-in examination of *boxes* 1–6 in *D*. In these regions, the perivascular ICC were identified as the Ano1-positive cells with at least two processes extending from the cell body and with contacts of cellular components with the vessel wall. *Arrows* indicate the ICC cell bodies (*yellow*: type I; *magenta*: type II perivascular ICC). NOTE. Specimens for Ano1 staining were prepared by cryosectioning and fixed in 25% acetic acid-75% ethanol (vol/vol) solution before the blocking and immunostaining procedure.

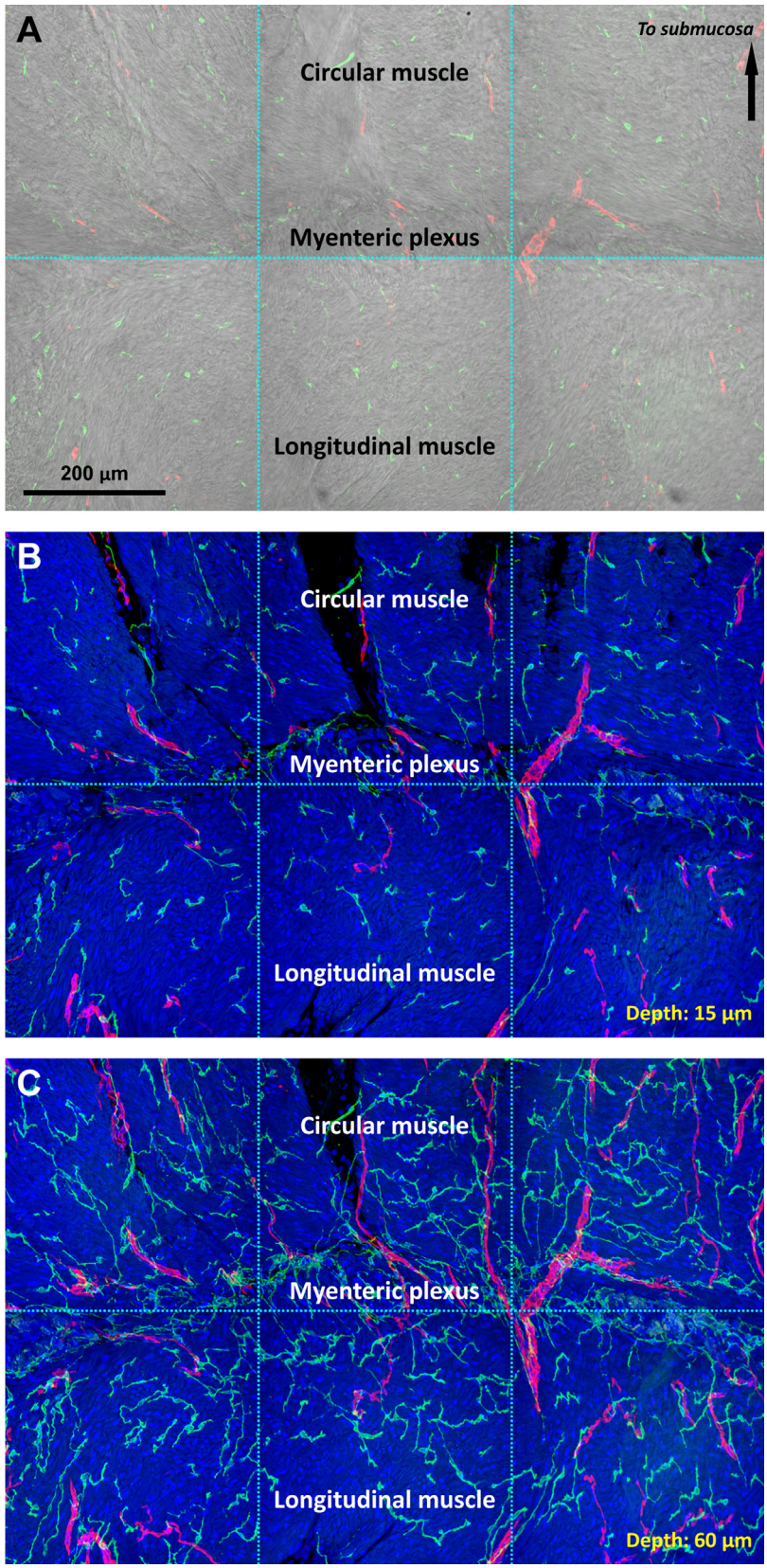

Figure 11. Ano1-labeled ICC imaged with different tissue depths to compare the acquired signals. (*A*) Overlay of the transmitted light and confocal image. The confocal optical section is at 5 μm. *Red*: CD31. *Green*: Ano1. *Blue*: nuclear staining and tissue autofluorescence. (*B*) Projection of the Ano1-labeled ICC with a depth of 15 μm. The acquired ICC signals are comparable to those of the standard immunohistochemistry. (*C*) Projection of the Ano1-labeled ICC with a depth of 60 μm. The increased tissue depth allows more signals to be collected for ICC network characterization.

References

1. Huizinga JD, Zarate N, Farrugia G. Physiology, injury, and recovery of interstitial cells of Cajal: basic and clinical science. Gastroenterology 2009;137:1548–1556.
2. Hirst GD, Ward SM. Interstitial cells: involvement in rhythmicity and neural control of gut smooth muscle. J Physiol 2003;550:337–346.
3. Sanders KM, Koh SD, Ward SM. Interstitial cells of cajal as pacemakers in the gastrointestinal tract. Annu Rev Physiol 2006;68:307–343.
4. Huizinga JD, Lammers WJ. Gut peristalsis is governed by a multitude of cooperating mechanisms. Am J Physiol Gastrointest Liver Physiol 2009;296:G1–G8.
5. Ward SM. Interstitial cells of Cajal in enteric neurotransmission. Gut 2000;47(Suppl 4):iv40–iv43.
6. Klein S, Seidler B, Kettenberger A, et al. Interstitial cells of Cajal integrate excitatory and inhibitory neurotransmission with intestinal slow-wave activity. Nat Commun 2013;4:1630.
7. Duthie HL. Electrical activity of gastrointestinal smooth muscle. Gut 1974;15:669–681.
8. Waterfall WE, Duthie HL, Brown BH. The electrical and motor actions of gastrointestinal hormones on the duodenum in man. Gut 1973;14:689–696.
9. Patterson LM, Zheng H, Ward SM, Berthoud HR. Immunohistochemical identification of cholecystokinin A receptors on interstitial cells of Cajal, smooth muscle, and enteric neurons in rat pylorus. Cell Tissue Res 2001; 305:11–23.
10. Glatzle J, Sternini C, Robin C, et al. Expression of 5-HT3 receptors in the rat gastrointestinal tract. Gastroenterology 2002;123:217–226.
11. Liu M, Geddis MS, Wen Y, et al. Expression and function of 5-HT4 receptors in the mouse enteric nervous system. Am J Physiol Gastrointest Liver Physiol 2005;289: G1148–G1163.
12. Wouters MM, Farrugia G, Schemann M. 5-HT receptors on interstitial cells of Cajal, smooth muscle and enteric nerves. Neurogastroenterol Motil 2007;19(Suppl 2):5–12.
13. Maeda H, Yamagata A, Nishikawa S, et al. Requirement of c-kit for development of intestinal pacemaker system. Development 1992;116:369–375.
14. Ward SM, Burns AJ, Torihashi S, Sanders KM. Mutation of the proto-oncogene c-kit blocks development of interstitial cells and electrical rhythmicity in murine intestine. J Physiol 1994;480:91–97.
15. Ward SM, Burns AJ, Torihashi S, et al. Impaired development of interstitial cells and intestinal electrical rhythmicity in steel mutants. Am J Physiol 1995;269: C1577–C1585.
16. Huizinga JD, Thuneberg L, Kluppel M, et al. W/kit gene required for interstitial cells of Cajal and for intestinal pacemaker activity. Nature 1995;373:347–349.
17. Wouters MM, Gibbons SJ, Roeder JL, et al. Exogenous serotonin regulates proliferation of interstitial cells of Cajal in mouse jejunum through 5-HT2B receptors. Gastroenterology 2007;133:897–906.
18. Tharayil VS, Wouters MM, Stanich JE, et al. Lack of serotonin 5-HT2B receptor alters proliferation and network volume of interstitial cells of Cajal in vivo. Neurogastroenterol Motil 2010;22:462–469, e109–e110.
19. Horvath VJ, Vittal H, Ordog T. Reduced insulin and IGF-I signaling, not hyperglycemia, underlies the diabetes-associated depletion of interstitial cells of Cajal in the murine stomach. Diabetes 2005;54:1528–1533.
20. Forster J, Damjanov I, Lin Z, et al. Absence of the interstitial cells of Cajal in patients with gastroparesis and correlation with clinical findings. J Gastrointest Surg 2005; 9:102–108.
21. Grover M, Farrugia G, Lurken MS, et al. Cellular changes in diabetic and idiopathic gastroparesis. Gastroenterology 2011;140:1575–1585.e8.
22. He CL, Burgart L, Wang L, et al. Decreased interstitial cell of cajal volume in patients with slow-transit constipation. Gastroenterology 2000;118:14–21.
23. Wedel T, Spiegler J, Soellner S, et al. Enteric nerves and interstitial cells of Cajal are altered in patients with slow-transit constipation and megacolon. Gastroenterology 2002;123:1459–1467.
24. Kindblom LG, Remotti HE, Aldenborg F, Meis-Kindblom JM. Gastrointestinal pacemaker cell tumor (GIPACT): gastrointestinal stromal tumors show phenotypic characteristics of the interstitial cells of Cajal. Am J Pathol 1998;152:1259–1269.
25. Miettinen M, Lasota J. Gastrointestinal stromal tumors: review on morphology, molecular pathology, prognosis, and differential diagnosis. Arch Pathol Lab Med 2006; 130:1466–1478.
26. Fu YY, Lin CW, Enikolopov G, et al. Microtome-free 3-dimensional confocal imaging method for visualization of mouse intestine with subcellular-level resolution. Gastroenterology 2009;137:453–465.
27. Chiu YC, Hua TE, Fu YY, et al. 3-D imaging and illustration of the perfusive mouse islet sympathetic innervation and its remodelling in injury. Diabetologia 2012; 55:3252–3261.
28. Hua TE, Yang TL, Yang WC, et al. 3-D neurohistology of transparent tongue in health and injury with optical clearing. Front Neuroanat 2013;7:36.
29. Fu YY, Tang SC. At the movies: 3-dimensional technology and gastrointestinal histology. Gastroenterology 2010;139:1100–1105.
30. Fu YY, Tang SC. Optical clearing facilitates integrated 3D visualization of mouse ileal microstructure and vascular network with high definition. Microvasc Res 2010; 80:512–521.
31. Liu YA, Chen Y, Chiang AS, et al. Optical clearing improves the imaging depth and signal-to-noise ratio for digital analysis and three-dimensional projection of the human enteric nervous system. Neurogastroenterol Motil 2011;23:e446–e457.
32. Liu YA, Chung YC, Pan ST, et al. 3-D imaging, illustration, and quantitation of enteric glial network in transparent human colon mucosa. Neurogastroenterol Motil 2013;25:e324–e338.
33. Fu YY, Peng SJ, Lin HY, et al. 3-D imaging and illustration of mouse intestinal neurovascular complex. Am J Physiol Gastrointest Liver Physiol 2013;304: G1–G11.

34. Liu YA, Chung YC, Pan ST, et al. 3-D illustration of network orientations of interstitial cells of Cajal subgroups in human colon as revealed by deep-tissue imaging with optical clearing. Am J Physiol Gastrointest Liver Physiol 2012;302:G1099–G1110.
35. Liu YA, Pan ST, Hou YC, et al. 3-D visualization and quantitation of microvessels in transparent human colorectal carcinoma. PLoS One 2013;8:e81857.
36. Caputo A, Caci E, Ferrera L, et al. TMEM16A, a membrane protein associated with calcium-dependent chloride channel activity. Science 2008;322:590–594.
37. Hwang SJ, Blair PJ, Britton FC, et al. Expression of anoctamin 1/TMEM16A by interstitial cells of Cajal is fundamental for slow wave activity in gastrointestinal muscles. J Physiol 2009;587:4887–4904.
38. Zhu MH, Kim TW, Ro S, et al. A Ca^{2+}-activated Cl^{-} conductance in interstitial cells of Cajal linked to slow wave currents and pacemaker activity. J Physiol 2009;587:4905–4918.
39. Kashyap P, Gomez-Pinilla PJ, Pozo MJ, et al. Immunoreactivity for Ano1 detects depletion of Kit-positive interstitial cells of Cajal in patients with slow transit constipation. Neurogastroenterol Motil 2011;23:760–765.
40. Sanders KM, Ordog T, Koh SD, et al. Development and plasticity of interstitial cells of Cajal. Neurogastroenterol Motil 1999;11:311–338.
41. Komuro T. Structure and organization of interstitial cells of Cajal in the gastrointestinal tract. J Physiol 2006;576:653–658.
42. Vanderwinden JM, Rumessen JJ. Interstitial cells of Cajal in human gut and gastrointestinal disease. Microsc Res Tech 1999;47:344–360.
43. Giugliano D, Ceriello A, Paolisso G. Oxidative stress and diabetic vascular complications. Diabetes Care 1996;19:257–267.
44. Feihl F, Liaudet L, Levy BI, Waeber B. Hypertension and microvascular remodelling. Cardiovasc Res 2008;78:274–285.
45. Chung K, Deisseroth K. CLARITY for mapping the nervous system. Nat Methods 2013;10:508–513.
46. Tang SC, Peng SJ, Chien HJ. Imaging of the islet neural network. Diabetes Obes Metab 2014;16(Suppl 1):77–86.
47. Tang SC, Chiu YC, Hsu CT, et al. Plasticity of Schwann cells and pericytes in response to islet injury in mice. Diabetologia 2013;56:2424–2434.
48. Juang JH, Peng SJ, Kuo CH, Tang SC. Three-dimensional islet graft histology: panoramic imaging of neural plasticity in sympathetic reinnervation of transplanted islets under the kidney capsule. Am J Physiol Endocrinol Metab 2014;306:E559–E570.
49. Cianchi F, Cortesini C, Bechi P, et al. Up-regulation of cyclooxygenase 2 gene expression correlates with tumor angiogenesis in human colorectal cancer. Gastroenterology 2001;121:1339–1347.
50. Wilhelm SM, Carter C, Tang L, et al. BAY 43-9006 exhibits broad spectrum oral antitumor activity and targets the RAF/MEK/ERK pathway and receptor tyrosine kinases involved in tumor progression and angiogenesis. Cancer Res 2004;64:7099–7109.

Received June 8, 2014. Accepted November 12, 2014.

Correspondence
Address correspondence to: Shiue-Cheng Tang, PhD, National Tsing Hua University, Department of Medical Science, 101, Section 2, Kuang Fu Road, Hsinchu 30013, Taiwan. e-mail: sctang@life.nthu.edu.tw; fax: (886) 3-571-5934.

Acknowledgments
The authors thank the Brain Research Center in the National Tsing Hua University for technical support in confocal imaging and postrecording image processing, and Dr. M. Schemann at Technical University of Munich for helpful suggestions.

Conflicts of interest
The authors disclose no conflicts.

Funding
This study was funded in part by grants from the joint research program between National Taiwan University Hospital, Hsinchu Branch, and National Tsing Hua University [Grant 102N2734E1] and the National Science Council [Grant NSC 102-2628-B-007-002-MY2] (to S.C.T.).